ChemPubSoc Europe

DOI: 10.1002/celc.201500536

CHEMELECTROCHEM Articles

Self-Sacrificial Template-Directed Synthesis of Metal–Organic Framework-Derived Porous Carbon for Energy-Storage Devices

Bing Ding, Jie Wang, Zhi Chang, Guiyin Xu, Xiaodong Hao, Laifa Shen, Hui Dou, and Xiaogang Zhang*[a]

Metal–organic framework (MOF)-derived carbon materials exhibit large surface areas, but dominant micropore characteristics and uncontrollable dimensions. Herein, we propose a self-sacrificial template-directed synthesis method to engineer the porous structure and dimensions of MOF-derived carbon materials. A porous zinc oxide (ZnO) nanosheet solid is selected as the self-sacrificial template and two-dimensional (2D) nanostructure-directing agent to prepare 2D ZIF-8-derived carbon nanosheets (ZCNs). The as-prepared ZCN materials exhibit a large surface area with hierarchical porosity. These intriguing features render ZCN materials advanced electrode materials for electrochemical energy-storage devices, demonstrating large ion-accessible surface area and high ion-/electron-transport rates. This self-sacrificial template-directed synthesis method offers new avenues for rational engineering of the porous structure and dimensions of MOF-derived porous carbon materials, thus exploiting their full potential for electrochemical energy-storage devices.

1. Introduction

Porous carbon materials, owing to their appealing properties of large surface area, high electric conductivity, and excellent chemical stability, can be used for a broad range of applications in electrochemical energy-storage devices, including supercapacitors and batteries.[1] To develop high-performance electrodes, various carbon materials with desired porous structures and morphologies have been extensively studied over the past few decades.[2] Recently, metal–organic framework (MOF)-derived carbon materials have emerged as promising candidates, owing to their unique characterizations.[3] MOF-derived carbon materials are prepared by direct pyrolysis of MOFs without any additional carbon sources or further activation. Owing to the highly uniform pores and designable organic species in MOFs, MOF-derived carbon materials usually exhibit large surface areas. To date, various MOF-derived carbon materials have been prepared from multiple types of MOFs.[3b,c,4] For example, direct pyrolysis of commercially available $Zn(MeIm)_2$ (ZIF-8; MeIm = 2-methylimidazole) powder or ZIF-8 microcrystals could produce porous carbon materials with Brunauer–Emmett–Teller (BET) surface areas up to 800–1610 $m^2 g^{-1}$.[4b,d,f–h] When used as the electrode material for supercapacitors, the specific capacitance reaches 130 $F g^{-1}$ in aqueous electrolyte.[4b] ZIF-8-derived carbon materials are also potential sulfur immobilizers for lithium–sulfur (Li–S) batteries, which could confine sulfur species and improve the specific capacity and cycling stability of the sulfur electrode.[4g–i]

Although the advantages of MOF-derived carbon materials for energy-storage applications have been highlighted a lot in previous reports, they still suffer from some drawbacks. Firstly, as electrode materials for electrochemical energy-storage devices, carbon materials with hierarchical porosity, typically mesopores in combination with micropores or macropores, are highly desirable.[5] MOF-derived carbon materials, however, normally exhibit dominant micropore characteristics, which limit ion diffusion, thus lowering the electrochemical performance, especially at high current density. Secondly, the dimensions of carbon materials are vital to the electrolyte permeability and ion-/electron-transport kinetics.[6] For instance, two-dimensional (2D) carbon with a high aspect ratio satisfies the requirements and manifests superior electrochemical performance.[7] In previous reports, great efforts have been devoted to synthesize MOF microcrystal or nanocrystal precursors, but rational control of the dimensions and porous structure of MOF-derived carbons are lacking. It is still a challenge to control the dimensions of MOF-derived carbon materials, especially synthesis of 2D MOF-derived carbons. Recently, the template-assistant strategy was developed to address the challenges of MOF-derived carbon.[8] Yu and co-workers described a tellurium nanowire-derived templating synthesis of ZIF-8 nanofibers and ZIF-8 nanofiber-derived carbon nanofibers.[8a] The carbon nanofibers exhibited a large specific area of 2270 $m^2 g^{-1}$ and excellent performance for the oxygen reduction reaction. However, the high production costs and limited scalability of the template restricts the wide application of MOF-derived carbon materials. In addition, to confine the

[a] B. Ding, J. Wang, Z. Chang, G. Xu, X. Hao, Dr. L. Shen, Prof. H. Dou, Prof. X. Zhang
Jiangsu Key Laboratory of Materials and Technology for Energy Conversion
College of Material Science and Engineering
Nanjing University of Aeronautics and Astronautics
Nanjing, 210016 (P. R. China)
E-mail: azhangxg@nuaa.edu.cn

Supporting Information for this article can be found under http://dx.doi.org/10.1002/celc.201500536.

growth of MOFs on the surface, some templates need further surface modification.[8b,c]

An alternative strategy is the self-sacrificing template method, which fabricates desired nanostructures through sacrificing the template themselves and initiating the growth process without any surface modification.[9] Inspired by this, a self-sacrificial template-directed synthesis method was proposed to engineer the porous structure and dimensions of MOF-derived carbon materials. In this work, for the convenience of concept demonstration, a porous zinc oxide (ZnO) nanosheet solid was selected as the self-sacrificial template and 2D nanostructure-directing agent to prepare 2D ZIF-8-derived carbon nanosheets (ZCNs). The as-prepared carbon nanosheets exhibit graphene-like morphology and a large surface area with hierarchical porosity. ZCNs with these unique characterizations exhibit advanced performances as electrode materials for supercapacitors and Li–S batteries.

2. Results and Discussion

Our method to control the porous structure and dimensions of ZIF-8-derived carbon is based on the self-sacrificing template synthesis. As schematically presented in Figure 1 a, porous ZnO nanosheets were used as the self-sacrificial template and 2D nanostructure-directing agent. Firstly, with the assistance of solvents and MeIm, Zn^{2+} was released from ZnO, which then initiates the in situ growth of ZIF-8 on the surface of ZnO. A ZIF-8@ZnO core–shell nanostructure was produced in this procedure. During the subsequent carbonization process, pyrolysis of the ZIF-8 shell leaves a microporous carbon wall. Simultaneously, the carbothermal reduction of the ZnO core and vaporization of Zn metal created dense mesopores, thus obtaining 2D carbon nanosheets with a hierarchically porous nanostructure. In particular, the thickness of the carbon wall and the size of mesopores could be adjusted by controlling the growth time of ZIF-8 shell. The ZIF-8-derived carbon nanosheets are denoted ZCNs-*n*, where *n* represents the growth time of ZIF-8 (4 and 12 h).

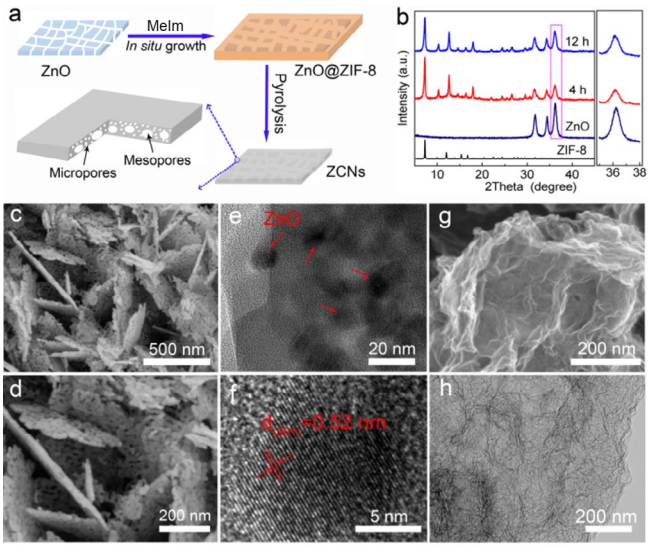

Figure 1. a) Schematic illustration of self-sacrificial template-directed synthesis of ZCNs, where ZnO acts as both the Zn^{2+} resource for initial growth of ZIF-8 and self-sacrificial template for the formation of mesopores. ZCNs show a porous structure combined with microspores and mesopores. b) XRD patterns of ZnO nanosheets and ZnO@ZIF-8 composites; the peaks corresponding to ZnO (101) reflections are highlighted in the right column. c, d) SEM images of ZnO nanosheet template. e) TEM and f) HRTEM images of ZnO@ZIF-8 composite. g) SEM and h) TEM images of ZCNs-4.

To track the formation process of the hierarchical porous 2D carbon nanosheets, time-dependent reactions were carried out and the structures and morphologies of the products were characterized. The successful preparation of the ZnO@ZIF-8 precursor was firstly confirmed by using powder X-ray diffraction (XRD). The XRD patterns reveal that ZnO@ZIF-8 precursors prepared with different reaction times are the composites of ZnO and ZIF-8 (Figure 1 b). The main peaks and relative intensity agree well with those of ZnO and simulated ZIF-8. As highlighted in the right column, compared with ZnO template, the (101) peaks of ZnO in ZnO@ZIF-8 precursors are lower in intensity and wider in the full width at half maximum. These changes indicate that the content and size of ZnO nanoparticles decreased. Scanning electron microscopy (SEM) images display that the ZnO nanosheets are composed of interconnected nanoparticles with size of 40–50 nm (Figures 1 c and 1 d). The thickness is approximately 15 nm. After growth for 4 h, the interparticle pores were completely occupied by ZIF-8 and the nanosheets became thicker (Figure S1). With a prolonged growth time of 12 h, the nanosheets became much thicker and tended to aggregate. In the SEM images, ZIF-8 polyhedrons were not observed, verifying the directed-growth of ZIF-8 along the surface of the ZnO nanosheets. Transmission electron microscopy (TEM) and high-resolution TEM (HRTEM) images confirm the core–shell structure of ZnO@ZIF-8 (Figures 1 e and 1 f). ZnO nanoparticles were completely embedded in the ZIF-8 and the size of ZnO nanoparticles decreases to 10–15 nm. Moreover, the ZIF-8 was quite compact and no cracks were observed.

2D carbon nanosheets were obtained through the direct pyrolysis of the ZnO@ZIF-8 precursor without any chemical activation or template etching process. Thermogravimetric analyses (TGA) were performed to investigate the carbonization process (Figure S2). The first step is attributed to the pyrolysis of ZIF-8 between 500 and 600 °C, whereas the second step above 700 °C is indicative of the carbothermal reduction of ZnO.[4f,10] So, the carbonization process was set at 950 °C and held for 10 h, ensuring the complete reduction of ZnO and vaporization of Zn. The XRD pattern and Raman spectra confirm that no ZnO or Zn-metal impurities remained in the as-prepared carbon (Figure S3). In the XRD pattern, two broad peaks located around 25° and 44° were assigned to the characteristic carbon (002) and (100) diffractions, respectively, revealing the presence of long-range 2D ordering in the carbon matrices along with some graphitization. The Raman spectra of ZCNs-4 present a D band at 1359 cm^{-1} and a G band at1602 cm^{-1}, which are related to defects and graphitization, respectively. The high value of the intensity ratio I_D/I_G (1.07) of ZCNs-4 indicates a high graphitization degree. In addition, the shapes of the D and 2D bands (at approximately 2765 cm^{-1}) show fea-

tures of few-layered graphene.[3c,11] As revealed in the SEM images (Figure S4), the as-prepared carbon materials show graphene-like morphology with abundant crumples and interconnected macropores. We could observe that the carbon materials are composed of thin carbon nanosheets (Figures 1e,f). Moreover, it is worth mentioning that this synthesis method could also be used to fabricate ZIF-8-derived carbon materials with other unique nanostructures. By using ZnO spheres, we could prepare zero-dimensional (0D) ZIF-8-derived hollow carbon spheres (Figure S5). On the whole, all of these results support the self-sacrificial template-directed synthesis of ZIF-8-derived carbon materials with controllable dimensions.

As shown in Figures 2a,b, the TEM images clearly show that the 2D porous carbon nanosheets show a hierarchically porous nanostructure, constituting microporous walls and mesoporous hollows. It is noted that a highly porous structure with thin and unbroken carbon walls can be obtained. In addition, we

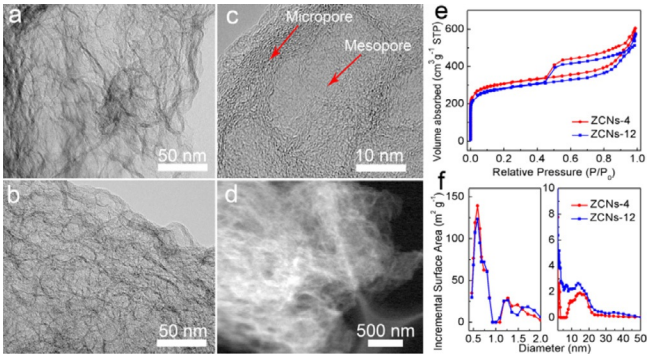

Figure 2. Structural and porous characterization of ZCNs-4 and ZCNs-12: TEM images of a) ZCNs-4 and b) ZCNs-12. c) HRTEM and d) STEM images of ZCNs-4. e) N_2 sorption isotherms and f) corresponding pore-size distribution curves of ZCNs-4 and ZCNs-12.

could observe that ZCNs-12 shows thicker carbon walls and are more compact. The HRTEM image shows carbon walls of less than 5 nm in thickness and abundant disordered graphene layers in ZCNs-4 (Figure 2c). The formation of hierarchical porosity is attributed to two factors: 1) as widely reported in previous reports, carbonization of ZIF-8 will lead to highly microporous carbon;[3a,4b] 2) the reduction of ZnO nanoparticles by the consumption of carbon atoms and vaporization of Zn metal creates dense mesopores in the interior of carbon nanosheets.[4a,10] The STEM image further confirms the hierarchically porous nanostructure distributed in the interconnected thin carbon nanosheets.

A nitrogen adsorption experiment was further performed to examine the pore characteristics of the 2D carbons nanosheets. The N_2 sorption isotherms of ZCNs-4 and ZCNs-12 both exhibit characteristics of type I/IV (Figure 2e). The steep adsorption at low relative pressure indicates a high number of micropores and the hysteresis loop at high relative pressure suggests the formation of a mesoporous structure, confirming the hierarchically porous structure of ZCNs. The BET surface area (S_{BET}) of ZCNs-4 and ZCNs-12 are as high as 1228 and 1023 $m^2 g^{-1}$, respectively. Furthermore, a notable feature of high ratio of the meso-/macropore volume to micropore volume ($V_{meso+macro}/V_{micro}$) was observed. For ZCNs-4 and ZCNs-12, the $V_{meso+macro}/V_{micro}$ ratios are up to 2.46 and 2.22, respectively, which are much higher than that of ZIF-8-derived carbon.[3b,4b,12] According to the non-local density functional theory (NLDFT) model, ZCNs-4 and ZCNs-12 show similar microporous distributions with maximum frequencies near 0.6 and 1.3 nm, respectively (Figure 2f). However, the mesopores in ZCNs-12 are smaller than ZCNs-4. This is because the longer time growth of ZIF-8 shells leaves a smaller ZnO core.

To evaluate the chemical identities of the heteroatoms in the ZCNs materials, X-ray photoelectron spectroscopy (XPS) and X-ray absorption near-edge structure (XANES) measurements were carried out. XPS confirmed that ZCNs-4 exhibits a predominant peak at 284.7 eV corresponding to C1s, 531.4 eV to O1s, and 399.5 eV to N1s (Figure S6). The atomic concentration of N in ZCNs-4 is up to 4.64%. The high-resolution C1s spectrum of ZCNs-4 can be deconvoluted into three individual component peaks, corresponding to C=C sp^2 (284.6 eV), C–C sp^3 (285.7 eV), and C–O/C–N (286.6 eV) (Figure 3a).[4f] The ratio of C=C/C–C was up to 96%, indicating

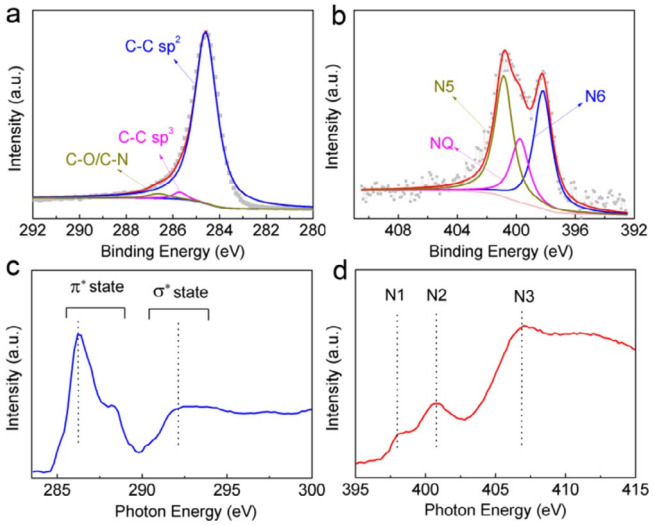

Figure 3. a) High-resolution C1s and b) N1s XPS spectra of ZCNs-4. c) C-K edge and d) N-K edge XANES spectra of ZCNs-4.

a high graphitization degree. The N1s spectrum (Figure 3b) can be fitted to three peaks located at 400.8, 399.7, and 398.2 eV, which are attributed to quaternary (N-Q), pyrrolic (N-5), and pyridinic (N-6) nitrogen, respectively.[3c,4f] As shown in the C-K edge XANES, peaks C1and C2 at around 285 and 292.4 eV are attributed to C–C π* (ring) and C–C σ* (ring) transitions, respectively (Figure 3c).[13] The high intensity of the C1 peak further confirms the high graphitization degree of ZCNs-4. The adsorptions in the 286–290 eV region correspond to carbon atoms that are attached to either oxygen or nitrogen atoms. In the N-K XANES spectra, three well-resolved resonance peaks located at N1 (ca. 397.9 eV), N2 (ca. 400.7 eV), and N3 (ca. 406.8 eV) are observed. Peak N1 and N3 are attributed

to the pyridinic (C=N π*) and graphitic-type nitrogen species, respectively. Peak N2 is assigned to general transitions from the N 1s core level to C–N s* states.[13] The XPS and XANES results proved that the carbon materials prepared by this self-sacrificial template-directed synthesis show a high graphitization degree and high-level nitrogen doping.

The unique 2D nanostructure, high-level nitrogen doping, and expected large surface area with hierarchical porosity render ZCNs advanced electrode materials for supercapacitors, which showcase significant advantages of high power density and long cycling life.[6] Figure 4 shows the electrochemical

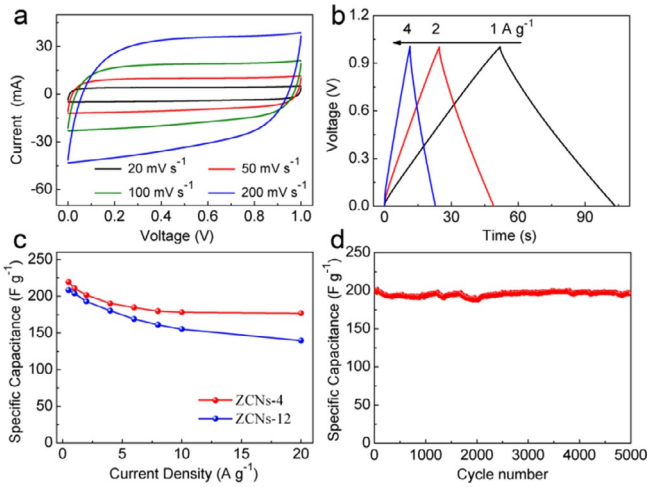

Figure 4. Electrochemical performance of ZCNs electrodes: a) CV curves of ZCNs-4 at various scanning rates; b) galvanostatic charge/discharge curves under various current densities for ZCNs-4; c) specific capacitance dependence on current density of ZCNs-4 and ZCNs-12; d) long-term cycle stability of ZCNs-4 at a current density of 2 A g^{-1}.

characterization results of the ZCN electrode in 6 M KOH aqueous electrolyte with a symmetrical two-electrode system. Rectangular cyclic voltammetry (CV) curves of ZCNs-4 are presented in Figure 4a. It can be seen that the CV curves display an almost rectangular shape even at 200 mV s^{-1}, highlighting typical supercapacitive behavior. The galvanostatic charge/discharge curves of ZCNs-4 at different current densities exhibit a symmetric triangle feature without an obvious potential drop (Figure 4b), further indicting efficient charge transfer within the ZCNs-4 electrode. Figure 4c compares the calculated specific capacitances of the ZCNs-4 and ZCNs-12 electrodes at different current densities. At a current density of 0.5 A g^{-1}, the specific capacitances of ZCNs-4 and ZCNs-12 are up to 220 and 208 F g^{-1}, respectively. The high specific capacitances may be attributed to the large ion-accessible surface area for forming an electrical double layer and a pseudocapacitive contribution of the nitrogen-containing functional groups.[4b,14] With increasing current density, the ZCNs-4 electrode manifests a higher specific capacitance than ZCNs-12. At 20 A g^{-1}, ZCNs-4 still exhibits a specific capacitance of 177 F g^{-1}, exhibiting excellent rate capability.

The supercapacitive performance of ZCNs-4 was further analyzed by using electrochemical impedance spectroscopy (EIS). ZCNs-4 clearly shows a lower charge-transfer resistance and ion-transport resistance (Figure S7a). In addition, the ZCNs-4 device shows a lower time constant, τ_0, of 1.28 s compared to that of the ZCNs-12 electrode (2.94 s) (Figure S7b). The lower time constant clearly demonstrates the crucial role of thinner carbon walls in greatly promoting ion kinetics in the interior of the electrodes. Significantly, in terms of specific capacitance and rate capability, the ZCNs-4 electrode shows greatly improved performances compared to ZIF-8 microcrystal-derived carbon materials and are comparable with other advanced 2D carbon materials.[12,15] All of these results indicate that ZCNs-4 shows a greatly improved performance, which could be attributed to its unique 2D porous nanostructure and high-level nitrogen doping. This nanostructure not only ensures fast ion diffusion by shortening the diffusion pathways, but also provides continuous electron pathways. In addition, nitrogen doping improves the electrical conductivity and wettability, and thus further enhances the ion-transfer efficiency. ZCNs-4, with a higher $V_{meso+macro}/V_{micro}$ volume ratio and thinner nanosheets structures, offers faster ion-transport channels, resulting in a higher capacitance retention at high current density. Furthermore, ZCNs-4 also exhibits excellent cycling performance, possessing a high capacitance retention of over 97% after 5000 galvanostatic charge/discharge cycles at 2 A g^{-1} (Figure 4d).

The large-surface-area, unique, 2D nanostructure with microporous walls, mesoporous hollows, and high-level nitrogen doping also make ZCNs advanced sulfur immobilizers for Li–S batteries, which showcase significant advantages of high energy density (1600 Wh kg^{-1}) and low cost.[16] As shown in SEM image (Figure 5a), the encapsulation of sulfur into the ZCNs-4 induced no obvious changes in morphology. No bulk sulfur particles or aggregations were detected on the external surface of the ZCNs-4. The TEM images in Figure 5b indicate

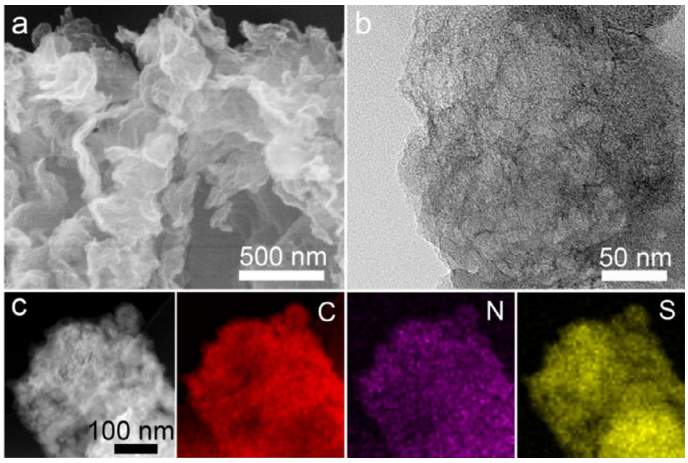

Figure 5. Structural characterization of the ZCNs-4/S composite: a) SEM images; b) TEM images; c) STEM image and corresponding elemental mapping.

that the sulfur is homogeneously dispersed in the porous carbon matrix. The STEM image and corresponding element mapping also indicate the homogeneous dispersion of sulfur in the ZCNs-4 matrix (Figure 5c). Raman spectra further confirm the good distribution of incorporated sulfur (Figure S8). The absence of a peak for sulfur indicates that sulfur is confined within the pores and shows an amorphous structure. Intimate contact between the sulfur and graphene layers is critical for rapid electron transport. A sulfur loading of approximately 60 wt% was determined by using TGA (Figure S9). Meanwhile, two steps in the sulfur evaporation process are observed for the ZCNs-4/S composite, indicating that elemental sulfur is incorporated not only in the microporous carbon wall, but also in the internal mesopores.[17]

The CV profile of the ZCNs-4/S electrode shows three peaks in the cathodic scan and one peak in the anodic scan (Figure S10). According to the reported mechanisms for the reduction and oxidation of sulfur during the charge/discharge process, the first peak at 2.4 V corresponds to the reduction of elemental sulfur to long-chain lithium polysulfides (Li_2S_n, $4 \leq n \leq 8$). The second peak at 2.04 V corresponds to further reduction of the long-chain lithium polysulfides to Li_2S_2/Li_2S. The reduction peak below 1.7 V corresponds to the reduction of small sulfur molecules (from $S_{2\approx4}$ to Li_2S_2/Li_2S), which was confined in the microporous carbon wall. The oxidation peak at 2.33 V is attributed to the conversion of Li_2S_2/Li_2S to polysulfides.[18] At a current density of 0.5 C, after one cycle of activation, the ZCNs-4/S electrode shows a specific capacity of 931 mAh g^{-1} at the second cycle (Figure 6a). After 100 cycles, the ZCNs-4/S

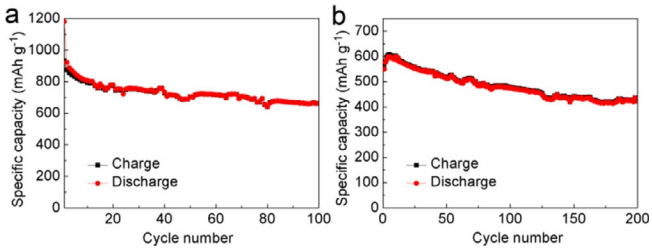

Figure 6. Cycling performance of ZCNs-4/S electrodes at a) 0.5 and b) 1 C.

electrode still delivers a specific capacity of 663 mAh g^{-1}. At a current density of 1 C, after 200 cycles, the specific capacity is up to 450 mAh g^{-1}, showing that the 2D porous host suspends the dissolution of lithium polysulfides during the charge/discharge process (Figure 6b). Comparatively, the ZCNs-12/S electrode shows a lower specific capacity and poorer cycling performance. The ZCNs-12/S electrode only derivers a specific capacity of 412 mAh g^{-1} after 100 cycles (Figure S11a and S11b). This may be attributed to the low surface area and more compact structure of ZCNs-12. To further investigate the roles of 2D porous carbon, capacity contributions from three discharge plateaus were distinguished from the potential profiles of the ZCNs-4/S electrode (Figure S11c and S11d). The extent of dissolution of polysulfides could lead to a decay of the capacity contribution from the upper discharge plateau.[19] The capacity retention of the upper plateau of the ZCNs-4/S composite was 70% after 100 cycles at 0.5 C. The high capacity retention can be attributed to the unbroken microporous carbon wall and lithium polysulfide binding capability of the nitrogen functional groups, suppressing the dissolution and shuttle of polysulfides.[20] This method provides a new possibility to prepare advanced sulfur immobilizers for long-term Li–S batteries.

3. Conclusions

A self-sacrificial template-directed synthesis method was developed for controlling the porous structure and dimensions of ZIF-8-derived carbon materials. By using porous ZnO nanosheets as the self-sacrificial template and 2D nanostructure-directing agent, 2D ZIF-8-derived carbon nanosheets could be obtained through the direct pyrolysis of a core–shell nanostructured ZnO@ZIF-8 precursor. The as-prepared 2D ZCN materials exhibit a high graphitization degree, large surface area, and unique hierarchical porosity, showing promising potential for electrochemical energy-storage devices. When used as the electrode for supercapacitors, the ZCNs-4 electrode exhibits an outstanding specific capacity of 220 F g^{-1} at 0.5 A g^{-1}, and remains 177 F g^{-1} at 20 A g^{-1}. Meanwhile, the unique properties make ZCNs an advanced sulfur immobilizer for improving the electron/ion transport and suppressing the dissolution and shuttle of polysulfides. We believe that the 0D and 2D nanostructures achieved by using porous ZnO spheres and ZnO nanosheets, respectively, can be extended to other nanostructures by using other templates such as ZnO films, ZnO nanowires arrays, and cobalt oxide nanowires arrays. This versatile synthetic method enables MOF-derived porous carbons to exploit their full potential in energy-storage applications.

Experimental Section

Synthesis of ZCN Materials

In a typical synthesis, ZnO nanosheets (204 mg) were added to *N*,*N*-dimethylformamide/H_2O mixed solvent (80 mL; v/v ratio of 3:1) and stirred for 1 h. Then, 2-methylimidazole (206 mg) was added to the dispersion under magnetic stirring. After stirring for 5 min, the homogeneous dispersion was added to Teflon-lined stainless-steel autoclave (100 mL). The autoclave was transferred to an oven. After the mixture was reacted for 4 and 12 h at 70 °C, the white product was collected by centrifugation and subsequently washed with fresh DMF and ethanol five times. The as-prepared ZnO@ZIF-8 composite was put into a crucible and transferred into a temperature-programmed furnace, and then heated to 200 °C for 6 h at a heating rate of 5 °C min^{-1}. A further pyrolysis treatment was performed at 950 °C for 10 h at a heating rate of 2 °C min^{-1}.

Preparation of the ZCNs-4/S Composite

The ZCNs-4/S composite was prepared through a melt–diffusion strategy. Typically, ZCNs-4 and elemental sulfur were mixed together and placed in a crucible, and then the mixture was heated to 155 °C and kept at that temperature for 20 h.

Characterization

XRD was studied by using a Bruker D8 Advance X-ray diffractometer with Cu Kα radiation. The morphologies were characterized by using a scanning electron microscope (Hitachi 4800) and a transmission electron microscope (Tecnai G2 F20). Raman spectroscopy was conducted on the HORIBA Scientific LabRAM HR Raman spectrometer system with a 532.4 nm laser. TGA was conducted on a TG-DSC instrument (NETZSCH STA 409 PC) under nitrogen protection. XPS analysis was performed on a PerkinElmer PHI 550 spectrometer with Al Kα (1486.6 eV) as the X-ray source. XANES spectra at the C K-edge and N K-edge were collected on beamline 08U at the Shanghai Synchrotron Radiation Facility (SSRF). The N_2 adsorption–desorption isotherms of the samples were measured by using a Micromeritics BK122T-B analyzer. The specific surface area was calculated using the BET method. The total pore volume and pore-size distribution were obtained from the NLDFT model.

Cell Fabrication and Measurements for Supercapacitors

The supercapacitor performances were measured by using a symmetric sandwich-type two-electrode system in 6 M KOH electrolyte. The electrodes were prepared by pressing a slurry of porous carbon nanosheets, carbon black, and polytetrafluoroethylene (PTFE) in a ratio of 80:15:5 onto a nickel foam current collector (1 × 1 cm^2) and then dried at 110 °C for 12 h. The active material mass loading for each electrode was about 2.5 mg cm^{-2}. A sandwich-type supercapacitor consisting of two similar sample electrodes was assembled. The CV, galvanostatic charge/discharge, and EIS tests were executed by using a CHI 660E electrochemical workstation. EIS was conducted in the frequency range of 10^5 Hz to 10^{-2} Hz with an amplitude of 5 mV. Galvanostatic charge/discharge cycling was performed on a CT2001A cell test instrument (LAND Electronic Co.). The gravimetric capacitance (*C*) was calculated based on Equation (1):

$$C = (4I\Delta t)/(m\Delta V) \quad (1)$$

where *I* is the constant discharge current, Δt is the discharge time, *m* is the total mass of two electrode materials, and ΔV represents the voltage range (excluding the *IR* drop).

Cell Fabrication and Measurements for Li–S Batteries

The ZCNs-4/S electrodes were prepared by using a slurry coating procedure. The slurry consisted of the ZCNs-4/S composite, acetylene black, and polyvinylidene fluoride (PVDF) in a weight ratio of 70:20:10 in *N*-methyl pyrrolidone, and was uniformly spread on an aluminum foil current collector and was then dried at 60 °C for 12 h. The active material loading was in the range of 0.6–0.8 mg cm^{-2}. CR2016-type coin cells were assembled in an argon-filled glove box. Lithium foil was used as the counter electrode and the separator was Celgard 2400. The electrolyte was composed of 1 M *bis*-(trifluoromethane) sulfonimide lithium (LiTFSI) salt and 0.1 M $LiNO_3$ additive dissolved in a mixed solvent of 1,3-dioxolane (DOL) and 1,2-dimethoxyethane (DME) (1:1 by volume). CV was performed on a CHI 660E electrochemical workstation. Galvanostatic charge/discharge cycling was performed on a CT2001A cell test instrument (LAND Electronic Co.).

Acknowledgements

The work was funded by the National Key Basic Research Program 973 (No. 2014CB239701), NSFC (No. 21173120, No. 51372116), Natural Science Foundation of Jiangsu Province (No. BK2011030, No. BK2011740, No. BK20151468), Fundamental Research Funds for the Central Universities of NUAA (NP2014403, NJ20140004) and Priority Academic Program Development of Jiangsu Higher Education Institutions (PAPD). B.D. is grateful to funding of Jiangsu Innovation Program for Graduate Education (CXZZ13 0158), Outstanding Doctoral Dissertation in NUAA (BCXJ13–13), and the Foundation of Graduate Innovation Center in NUAA (kfjj130219).

Keywords: electrochemistry · hierarchical porosity · metal–organic framework · self-sacrificial template · two-dimensional carbons

[1] a) P. Simon, Y. Gogotsi, *Acc. Chem. Res.* **2013**, *46*, 1094; b) F. Bonaccorso, L. Colombo, G. Yu, M. Stoller, V. Tozzini, A. C. Ferrari, R. S. Ruoff, V. Pellegrini, *Science* **2015**, *347*, 1246501.

[2] a) S. L. Candelaria, Y. Shao, W. Zhou, X. Li, J. Xiao, J.-G. Zhang, Y. Wang, J. Liu, J. Li, G. Cao, *Nano Energy* **2012**, *1*, 195; b) L. Hao, X. Li, L. Zhi, *Adv. Mater.* **2013**, *25*, 3899; c) Y. Zhu, S. Murali, M. D. Stoller, K. J. Ganesh, W. Cai, P. J. Ferreira, A. Pirkle, R. M. Wallace, K. A. Cychosz, M. Thommes, D. Su, E. A. Stach, R. S. Ruoff, *Science* **2011**, *332*, 1537; d) X. L. Ji, K. T. Lee, L. F. Nazar, *Nat. Mater.* **2009**, *8*, 500; e) Q. Sun, B. He, X.-Q. Zhang, A.-H. Lu, *ACS Nano* **2015**, *9*, 8504; f) J. T. Lee, Y. Zhao, S. Thieme, H. Kim, M. Oschatz, L. Borchardt, A. Magasinski, W.-I. Cho, S. Kaskel, G. Yushin, *Adv. Mater.* **2013**, *25*, 4573.

[3] a) J.-K. Sun, Q. Xu, *Energy Environ. Sci.* **2014**, *7*, 2071; b) J. Tang, R. R. Salunkhe, J. Liu, N. L. Torad, M. Imura, S. Furukawa, Y. Yamauchi, *J. Am. Chem. Soc.* **2015**, *137*, 1572; c) F. Zheng, Y. Yang, Q. Chen, *Nat. Commun.* **2014**, *5*, 5261.

[4] a) S. J. Yang, T. Kim, J. H. Im, Y. S. Kim, K. Lee, H. Jung, C. R. Park, *Chem. Mater.* **2012**, *24*, 464; b) W. Chaikittisilp, M. Hu, H. Wang, H. S. Huang, T. Fujita, K. C. Wu, L. C. Chen, Y. Yamauchi, K. Ariga, *Chem. Commun.* **2012**, *48*, 7259; c) S. Lim, K. Suh, Y. Kim, M. Yoon, H. Park, D. N. Dybtsev, K. Kim, *Chem. Commun.* **2012**, *48*, 7447; d) N. L. Torad, M. Hu, Y. Kamachi, K. Takai, M. Imura, M. Naito, Y. Yamauchi, *Chem. Commun.* **2013**, *49*, 2521; e) J.-W. Jeon, R. Sharma, P. Meduri, B. W. Arey, H. T. Schaef, J. L. Lutkenhaus, J. P. Lemmon, P. K. Thallapally, M. I. Nandasiri, B. P. McGrail, S. K. Nune, *ACS Appl. Mater. Interfaces* **2014**, *6*, 7214; f) L. Zhang, Z. Su, F. Jiang, L. Yang, J. Qian, Y. Zhou, W. Li, M. Hong, *Nanoscale* **2014**, *6*, 6590; g) K. Xi, S. Cao, X. Peng, C. Ducati, R. V. Kumar, A. K. Cheetham, *Chem. Commun.* **2013**, *49*, 2192; h) H. B. Wu, S. Wei, L. Zhang, R. Xu, H. H. Hng, X. W. Lou, *Chem. Eur. J.* **2013**, *19*, 10804; i) G. Y. Xu, B. Ding, L. F. Shen, P. Nie, J. P. Han, X. G. Zhang, *J. Mater. Chem. A* **2013**, *1*, 4490.

[5] a) S. Dutta, A. Bhaumik, K. C. W. Wu, *Energy Environ. Sci.* **2014**, *7*, 3574; b) D. W. Wang, F. Li, M. Liu, G. Q. Lu, H. M. Cheng, *Angew. Chem. Int. Ed.* **2008**, *47*, 373; *Angew. Chem.* **2008**, *120*, 379; c) M. Oschatz, L. Borchardt, K. Pinkert, S. Thieme, M. R. Lohe, C. Hoffmann, M. Benusch, F. M. Wisser, C. Ziegler, L. Giebeler, M. H. Ruemmeli, J. Eckert, A. Eychmueller, S. Kaskel, *Adv. Energy Mater.* **2014**, *4*, 1300645; d) T. Kim, G. Jung, S. Yoo, K. S. Suh, R. S. Ruoff, *ACS Nano* **2013**, *7*, 6899.

[6] a) X. Zheng, J. Luo, W. Lv, D. W. Wang, Q. H. Yang, *Adv. Mater.* **2015**, *27*, 5388; b) L. Dai, D. W. Chang, J.-B. Baek, W. Lu, *Small* **2012**, *8*, 1130.

[7] a) H. Wang, Z. Xu, A. Kohandehghan, Z. Li, K. Cui, X. Tan, T. J. Stephenson, C. K. King'ondu, C. M. Holt, B. C. Olsen, *ACS Nano* **2013**, *7*, 5131; b) X. Yang, L. Zhang, F. Zhang, Y. Huang, Y. Chen, *ACS Nano* **2014**, *8*, 5208; c) M. Q. Zhao, Q. Zhang, J. Q. Huang, G. L. Tian, J. Q. Nie, H. J. Peng, F. Wei, *Nat. Commun.* **2014**, *5*, 3410.

[8] a) W. Zhang, Z.-Y. Wu, H.-L. Jiang, S.-H. Yu, *J. Am. Chem. Soc.* **2014**, *136*, 14385; b) H. J. Lee, S. Choi, M. Oh, *Chem. Commun.* **2014**, *50*, 4492; c) H. X. Zhong, J. Wang, Y. W. Zhang, W. L. Xu, W. Xing, D. Xu, Y. F. Zhang, X. B. Zhang, *Angew. Chem. Int. Ed.* **2014**, *53*, 14235; *Angew.*

Chem. **2014**, *126*, 14459; d) J.-K. Sun, Q. Xu, *Chem. Commun.* **2014**, *50*, 13502.
[9] a) Y.-L. Ding, J. Xie, G.-S. Cao, T.-J. Zhu, H.-M. Yu, X.-B. Zhao, *Adv. Funct. Mater.* **2011**, *21*, 348; b) F. Zou, X. Hu, Z. Li, L. Qie, C. Hu, R. Zeng, Y. Jiang, Y. Huang, *Adv. Mater.* **2014**, *26*, 6622; c) E. Zanchetta, L. Malfatti, R. Ricco, M. J. Styles, F. Lisi, C. J. Coghlan, C. J. Doonan, A. J. Hill, G. Brusatin, P. Falcaro, *Chem. Mater.* **2015**, *27*, 690; d) W. W. Zhan, Q. Kuang, J. Z. Zhou, X. J. Kong, Z. X. Xie, L. S. Zheng, *J. Am. Chem. Soc.* **2013**, *135*, 1926.
[10] P. Strubel, S. Thieme, T. Biemelt, A. Helmer, M. Oschatz, J. Brückner, H. Althues, S. Kaskel, *Adv. Funct. Mater.* **2015**, *25*, 287.
[11] A. C. Ferrari, D. M. Basko, *Nat. Nanotechnol.* **2013**, *8*, 235.
[12] A. J. Amali, J. K. Sun, Q. Xu, *Chem. Commun.* **2014**, *50*, 1519.
[13] a) L.-S. Zhang, X.-Q. Liang, W.-G. Song, Z.-Y. Wu, *Phys. Chem. Chem. Phys.* **2010**, *12*, 12055; b) J. Zhong, J.-J. Deng, B.-H. Mao, T. Xie, X.-H. Sun, Z.-G. Mou, C.-H. Hong, P. Yang, S.-D. Wang, *Carbon* **2012**, *50*, 335.
[14] Z. Li, Z. Xu, X. Tan, H. Wang, C. M. B. Holt, T. Stephenson, B. C. Olsen, D. Mitlin, *Energy Environ. Sci.* **2013**, *6*, 871.
[15] H. Wang, L. Zhi, K. Liu, L. Dang, Z. Liu, Z. Lei, C. Yu, J. Qiu, *Adv. Funct. Mater.* **2015**, *25*, 5420.
[16] a) A. Manthiram, Y. Z. Fu, Y. S. Su, *Acc. Chem. Res.* **2013**, *46*, 1125; b) Y. Yang, G. Zheng, Y. Cui, *Chem. Soc. Rev.* **2013**, *42*, 3018; c) L. Xiao, Y. Cao, J. Xiao, B. Schwenzer, M. H. Engelhard, L. V. Saraf, Z. Nie, G. J. Exarhos, J. Liu, *Adv. Mater.* **2012**, *24*, 1176; d) C. Wu, L. Fu, J. Maier, Y. Yu, *J. Mater. Chem. A* **2015**, *3*, 9438.
[17] a) C. D. Liang, N. J. Dudney, J. Y. Howe, *Chem. Mater.* **2009**, *21*, 4724; b) J. Guo, Y. Xu, C. Wang, *Nano Lett.* **2011**, *11*, 4288; c) L. Zeng, F. Pan, W. Li, Y. Jiang, X. Zhong, Y. Yu, *Nanoscale* **2014**, *6*, 9579.
[18] a) Z. Li, Y. Jiang, L. Yuan, Z. Yi, C. Wu, Y. Liu, P. Strasser, Y. Huang, *ACS Nano* **2014**, *8*, 9295; b) S. Xin, L. Gu, N. H. Zhao, Y. X. Yin, L. J. Zhou, Y. G. Guo, L. J. Wan, *J. Am. Chem. Soc.* **2012**, *134*, 18510.
[19] a) N. Jayaprakash, J. Shen, S. S. Moganty, A. Corona, L. A. Archer, *Angew. Chem. Int. Ed.* **2011**, *50*, 5904; *Angew. Chem.* **2011**, *123*, 6026; b) G. Zhou, L.-C. Yin, D.-W. Wang, L. Li, S. Pei, I. R. Gentle, F. Li, H.-M. Cheng, *ACS Nano* **2013**, *7*, 5367; c) W. Kong, L. Sun, Y. Wu, K. Jiang, Q. Li, J. Wang, S. Fan, *Carbon* **2016**, *96*, 1053.
[20] a) J. Song, T. Xu, M. L. Gordin, P. Zhu, D. Lv, Y.-B. Jiang, Y. Chen, Y. Duan, D. Wang, *Adv. Funct. Mater.* **2014**, *24*, 1243; b) Y. Qiu, W. Li, W. Zhao, G. Li, Y. Hou, M. Liu, L. Zhou, F. Ye, H. Li, Z. Wei, S. Yang, W. Duan, Y. Ye, J. Guo, Y. Zhang, *Nano Lett.* **2014**, *14*, 4821.

Manuscript received: December 11, 2015
Accepted Article published: January 11, 2016
Final Article published: February 4, 2016